Unambiguous determination of the commensurate antiferromagnetic structure of $HoNi_2B_2C$ in the superconducting ground state

Andrew Sazonov,[1,*] Vladimir Hutanu,[1,†] Martin Meven,[1] Karine Röwer,[2,‡] Georg Roth,[2]
Eddy Lelièvre-Berna,[3] Günther Fuchs,[4] Oksana Zaharko,[5] and Karen Friese[6]

[1]*Institute of Crystallography, RWTH Aachen University and Jülich Centre for Neutron Science at Heinz Maier-Leibnitz Zentrum, D-85748 Garching, Germany*

[2]*Institute of Crystallography, RWTH Aachen University, D-52056 Aachen, Germany*

[3]*Institut Laue-Langevin, F-38042 Grenoble, France*

[4]*Leibniz-Institut für Festkörper- und Werkstoffforschung Dresden, D-01171 Dresden, Germany*

[5]*Laboratory for Neutron Scattering, ETH Zürich and Paul Scherrer Institute, CH-5232 Villigen, Switzerland*

[6]*Jülich Center for Neutron Science-2, Research Center Jülich GmbH, D-52425 Jülich, Germany*

(Received 23 September 2018; revised manuscript received 6 May 2019; published 12 July 2019)

Crystal and magnetic structures of the intermetallic $HoNi_2B_2C$ have been investigated using different single-crystal diffraction techniques at both room and low temperatures (superconducting phase). Combined refinement of the neutron and x-ray diffraction data performed at room temperature shows that the crystal structure of $HoNi_2B_2C$ is well described in the tetragonal space group $I4/mmm$, in agreement with the literature. The magnetic ordering at low temperatures is accompanied by a structural phase transition to the orthorhombic space group $Fmmm$. However, only noncharacteristic orbits are occupied in this space group, and the symmetry reduction is entirely due to a lifting of the symmetry-induced restrictions on the anisotropic displacement parameters. Based on magnetic symmetry analysis, two types of commensurate antiferromagnetic structures with different magnetic space groups (MSGs) are found below $T_N \approx 5.2$ K: MSG P_Innm (Ho spins are along the [100] direction of the parent structure) and MSG C_Amca (Ho spins are along [110] of the parent structure). Both models agree well with conventional unpolarized neutron diffraction data at low temperature (2.4 K) with ordered magnetic moments of 9.16(9) μ_B/Ho^{3+} atom. Spherical neutron polarimetry, on the other hand, allowed us to unambiguously solve the magnetic structure (MSG C_Amca) as well as to determine the population of two types of 90° antiferromagnetic domains (0.45/0.55).

DOI: 10.1103/PhysRevB.100.014414

I. INTRODUCTION

Quaternary intermetallics of the general composition RT_2B_2C (R = rare earth, T = transition metal) have attracted much interest in the last two decades due to their electronic, superconducting, and magnetic properties [1]. Superconducting transition temperatures T_c found for different R-based compounds vary from 0.1 K for $CeNi_2B_2C$ to 23 K for YPd_2B_2C [2,3]. The latter one is the highest known T_c for superconducting borocarbides. In many of these compounds the superconductivity coexists with long-range magnetic order. This coexistence has been attributed to the fact that the magnetic ions are well isolated from the conduction path, leading to very weak interactions between local magnetic moments and the conduction electrons [4].

The structures of the quaternary borocarbide compounds can be regarded as filled variants of the $ThCr_2Si_2$-type structure [5] and are generally described in the literature in the tetragonal space group (SG) $I4/mmm$ with approximated lattice parameters $a_{tet} = b_{tet} \approx 3.5$–$3.9$ Å and $c_{tet} \approx 9.8$–10.7 Å, depending on the individual compositions [6–9]. The structures consist of two types of layers: the inverse PbO-type Ni_2B_2 layer, in which the transition-metal atoms are tetrahedrally coordinated by four boron atoms, and the NaCl-type layer of RC, where each rare-earth atom is in square planar coordination with carbon and vice versa (see Fig. 1). The two layers are connected through a relatively rigid B-C bond which is aligned parallel to the crystallographic c axis. In the Lu compound the Ni_2B_2 layers are the least strained (and farthest apart). Since the electrons at the Fermi level are predominantly Ni $3d$ electrons, the straining of the Ni_2B_2 layer may strongly influence the superconducting behavior. Siegrist *et al.* [6] proposed that the B-Ni-B angle could be used as an indicator for possible superconductivity. The precise structural information would thus be very important to understand the functionality of each layer and its role in the occurrence of superconductivity. The large variety of magnetic structure types in the different nickel borocarbides in combination with the fact that magnetic order is highly influenced by the symmetry of the crystal structure suggests that even very small deviations (distortions) in the individual

*Present address: Data Management and Software Centre, European Spallation Source ERIC, DK-2200 Copenhagen, Denmark; Andrew.Sazonov@esss.se

†Vladimir.Hutanu@frm2.tum.de

‡Present address: CRELUX GmbH - a WuXi AppTec company, D-82152 Martinsried, Germany.

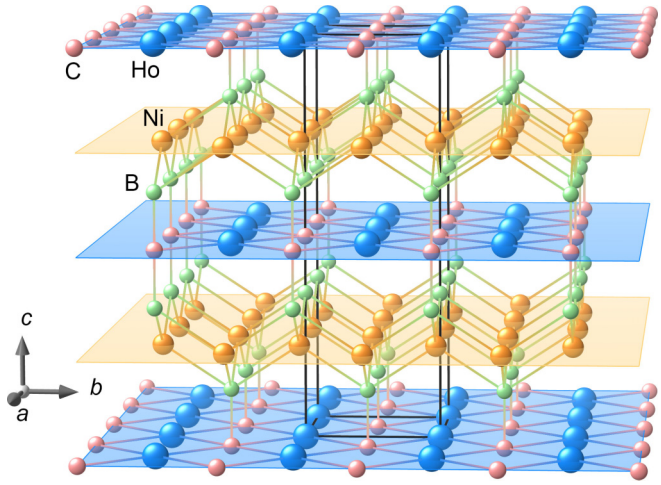

FIG. 1. Perspective view of the $HoNi_2B_2C$ crystal structure in SG $I4/mmm$. Blue and yellow planes perpendicular to the c axis correspond to the layers of Ho/C and Ni, respectively. Ho-C, B-C, and Ni-B distances are drawn for clarity.

crystal structures may lead to different electronic ordering processes which are at the origin of the superconductivity and/or the magnetic order. However, detailed crystallographic studies in the superconducting and/or magnetically ordered ground states are rather rare.

For investigating the fine interplay between superconducting and magnetic ordering parameters much attention has been focused on $HoNi_2B_2C$, where a series of open questions regarding both the crystal and magnetic structures persists despite the fact that it has been extensively studied in recent years [8,10–14]. This compound shows one of the most complex magnetic behaviors among the nickel borocarbides. It becomes superconducting at about 8.5 K. Between 6.2 and 5 K, the superconductivity is significantly suppressed, demonstrating near-reentrant resistive character. Below 5 K, $HoNi_2B_2C$ becomes superconducting again. It is noteworthy that in some samples the resistive reentrant behavior is observed even under zero field [4]. Also at about 8.5 K two families of magnetic peaks start to develop (see Ref. [14] and references therein), indicating the coexistence of a commensurate antiferromagnetic (AFM) structure with wave vector $\boldsymbol{k}_1 = (0, 0, 1)$ and an incommensurate, most likely spiral, state with $\boldsymbol{k}_2 = (0, 0, 0.911)$. Both the commensurate and incommensurate magnetic orders coexist with superconductivity. Additional magnetic peaks corresponding to a modulation wave vector $\boldsymbol{k}_3 = (0.586, 0, 0)$ develop below 6.25 K. At approximately the same temperature the incommensurate wave vector $\boldsymbol{k}_2$ starts to change and reaches a value of $\boldsymbol{k}_2 = (0, 0, 0.923)$ at 5.2 K [14]. Parallel to both incommensurate structures, further incommensurate reflections with wave vector $\boldsymbol{k}_4 = (0, 0, 0.904)$ develop in this temperature region (5–6.2 K). In many publications both $\boldsymbol{k}_2$ and $\boldsymbol{k}_4$ are denoted as one single incommensurate wave vector [10,13,15] due to the lack of instrumental resolution preventing the distinction of $\boldsymbol{k}_2$ and $\boldsymbol{k}_4$. However, high-resolution x-ray and neutron-scattering studies [16] clearly demonstrated that two independent phases coexist. Below about 5 K the incommensurate magnetic structures are suppressed, and only one commensurate antiferromagnetic phase with $\boldsymbol{k}_1$ is observed [10,15]. It has been proposed that the magnetic order is directly coupled to the superconducting order parameter [10,14].

In the commensurate AFM state below 5 K, different orientations are listed in the literature for the direction of the Ho magnetic moment. According to the first neutron powder diffraction experiments [10,11], the [100] axis was assumed. Later, the alignment along the [110] direction was suggested [8]. In both cases, in the low-temperature AFM phase which is the focus of this study, the magnetic moments of Ho are found to be coupled ferromagnetically in the ab plane. These ferromagnetic layers are then stacked antiferromagnetically along the c axis. It should be noted, however, that unpolarized neutron diffraction usually cannot unambiguously distinguish between those two types of magnetic structures. Moreover, it was suggested [17] that the Ho moments are canted by about 15° out of the ab plane.

In addition, detailed investigations on the temperature evolution of the $HoNi_2B_2C$ nuclear structure are missing, and to our knowledge, little is known about whether the magnetic transition is accompanied by a structural one. Weak orthorhombic distortion of the lattice (∼0.2%) in the direction of the magnetic moment due to magnetoelastic effects has been postulated for $HoNi_2B_2C$ in the AFM state on the basis of neutron powder diffraction measurements [18,19] in analogy to other nickel borocarbides, for example, $ErNi_2B_2C$ [19,20] and $TbNi_2B_2C$ [19,21]. However, the direction of the ordered magnetic moments seems to be different for those compounds, and no structural details (atomic positions and displacements) for the proposed orthorhombic phase have been presented. Finally, it is still not clear whether Ni atoms contribute to this magnetism or not.

Due to these open questions, we have decided to further investigate the commensurate antiferromagnetic and nuclear structures of $HoNi_2B_2C$ in the superconducting ground state (below 5 K), using single-crystal neutron diffraction techniques. Simultaneous refinement of single-crystal neutron and x-ray diffraction data was applied for precise structural determination at room temperature. Magnetic symmetry analysis was used to derive and test all possible magnetic space groups (MSGs), and the magnetic structure was refined using unpolarized single-crystal neutron diffraction data. Spherical neutron polarimetry (SNP) using a third-generation cryogenic polarization analysis device (CRYOPAD) was employed in order to obtain a unique solution for the magnetic moment orientation in the AFM state and to precisely determine the AFM domain populations [22].

II. EXPERIMENT

A high-quality single crystal of ^{11}B-substituted $HoNi_2B_2C$ was prepared using the high-temperature floating-zone technique as described in Refs. [23,24]. The quality of the raw materials used for crystal growth is specified elsewhere [25]. The sample was enriched with the ^{11}B isotope in order to reduce its absorption in the neutron studies.

The same sample of almost rectangular shape ($8 \times 4 \times 2$ mm^3) was used for both unpolarized and polarized neutron diffraction experiments. Smaller crystal pieces originating

from the large crystal were used for the x-ray diffraction measurements.

The single-crystal x-ray diffraction data were collected at room temperature using a STOE IPDS II diffractometer with Mo $K\alpha$ radiation at the Institute of Crystallography, RWTH Aachen University, Germany. Data were treated with the software package X-AREA [26].

Unpolarized single-crystal neutron diffraction was performed on the four-circle diffractometer HEiDi [27] at the hot source of the FRM II reactor at the Heinz-Maier-Leibnitz Zentrum (MLZ), Germany. Two wavelengths, $\lambda = 0.55$ Å and $\lambda = 0.79$ Å, were selected at room and low temperatures, respectively. A ^{3}He point detector, optimized for neutrons with short wavelengths, was used for these measurements. For the low-temperature experiments, the sample was wrapped in Al foil to ensure the homogeneity of its temperature and placed in a He closed-cycle cryostat mounted in the Eulerian cradle of the diffractometer. The temperature was measured and controlled by a diode sensor near the sample position, and a stability of 0.1 K was achieved.

The corrected integrated intensities of the measured reflections were obtained with the DAVINCI program [28] using a Gaussian peak fitting algorithm. Numerical absorption correction was performed with the TBAR program. Refinements of the structural parameters were performed with the program JANA2006 [29], in which both room-temperature x-ray and neutron single-crystal data were taken into account simultaneously.

Polarized neutron diffraction measurements were performed with the zero-field polarimeter CRYOPAD [30] on the polarized single-crystal diffractometer POLI [31] at the hot source of the FRM II reactor at MLZ. The wavelength $\lambda = 0.87$ Å was used in the spherical neutron polarimetry experiment. For this experiment, the sample was mounted with the [010] direction perpendicular to the scattering plane in a special "long-tail" FRM II closed-cycle cryostat, hosted inside the CRYOPAD. The good thermal coupling between the sample and the "cold finger" of the cryostat was ensured using a He-gas-filled sealed Al sample can. Stable temperatures down to 3.9 K were reached in the sample during the polarimetry experiment. The polarization of both the incoming and scattered beams was controlled by polarizing ^{3}He neutron spin filters. Since the filter polarization decays with time, this decay was controlled by a neutron transmission monitor for the incoming beam and by systematic polarization measurements of the (004) structural reflection for the scattered beam, similar to the procedure used in Ref. [13]. The appropriate polarization corrections were then applied, as given in Ref. [32].

For the refinement of the spherical polarimetry data the program SNPLSQ of the Cambridge Crystallography Subroutine Library [33] was used.

III. RESULTS AND DISCUSSION

A. Crystal structure at low temperature by single-crystal neutron diffraction

At room temperature $HoNi_2B_2C$ crystallizes in the tetragonal SG $I4/mmm$, and its crystal structure has been determined using combined refinement of the x-ray and neutron diffraction data. The results are presented in the Supplemental Material [34] and deposited in the crystallographic information file (CIF) [35].

In the neutron data of the magnetically ordered phase measured at 2.4 K, additional strong reflections with $h + k + l = 2n + 1$ ($n \in \mathbb{Z}$) in the tetragonal cell are clearly visible. To select an appropriate magnetic structure model it is important to know if those reflections are purely magnetic or if they have an additional nuclear contribution due to possible further symmetry lowering. In order to clarify this, we performed supplementary spherical neutron polarimetry measurements of the xx polarization matrix element on selected peaks (see Sec. III D for more details about the SNP technique). In the case of a pure nuclear reflection this element is expected to be $+1$. In our measurements those peaks with $h + k + l = 2n + 1$ ($n \in \mathbb{Z}$) are found to have the xx term close to -1, confirming the pure magnetic origin of the additional reflections. These peaks can be successfully indexed with the commensurate magnetic propagation vector $\boldsymbol{k} = (0, 0, 1)$. As a result, nuclear and magnetic Bragg reflections are separated from each other, and thus, the crystal structure was refined independently of the magnetic one. A total of 1029 nuclear Bragg reflections up to $\sin\theta/\lambda \approx 1.09$ Å^{-1} were measured with neutrons at 2.4 K.

Using high-resolution neutron powder diffraction [18,19], the splitting of the (220) and (332) nuclear reflections was observed in $HoNi_2B_2C$ below the magnetic transition temperature, whereas the shape of the (400) and (008) peaks remained unmodified. Such behavior was assigned to the orthorhombic magnetostrictive distortion along the [110] direction of the magnetic ordering in the basal plane. Similar magnetoelastic effects were also reported for other RNi_2B_2C compounds with $R =$ Dy and Tb [20,21]. In $HoNi_2B_2C$, $Fmmm$ is the only orthorhombic SG among the highest subgroups of the tetragonal SG $I4/mmm$, which is consistent with the observed splitting. We performed temperature-dependent scans (3.9–15 K) for a number of different Bragg reflections in order to observe the distortion. However, the small difference between the a and b lattice parameters of less than 0.2% suggested in Refs. [18,19] is at the limit of the angular resolution for a conventional single-crystal neutron diffractometer with short wavelengths. Therefore, we provide the refined structural parameters at low temperature (2.4 K) for two models: higher-symmetry tetragonal $I4/mmm$ ($a = b \approx 3.51$ Å, $c \approx 10.52$ Å), as found for $HoNi_2B_2C$ at room temperature, and lower-symmetry orthorhombic $Fmmm$ ($a' \approx b' \approx 4.96$ Å, $c' \approx 10.52$ Å), as suggested in Ref. [18] and following from the group-subgroup symmetry relations (see Table I). The particular differences and similarities between those two models are discussed in the Supplemental Material [34].

In both SGs $Fmmm$ and $I4/mmm$, Ni is surrounded by four B atoms at equal distances of 2.098(1)Å (see Fig. 2). Each C atom has two nearest B neighbors at 1.486(1)Å. The angles in the [NiB_4] tetrahedra vary from 107.32(1)° to 113.87(3)°. In Ref. [6], where the structures of different RT_2B_2C compounds were discussed on the basis of models in space group $I4/mmm$, it was assumed that the values of the B-Ni-B angles could be used as an indication of the presence or absence of the superconducting phases. Accordingly, only

TABLE I. Fractional atomic coordinates (x, y, z) and isotropic and anisotropic atomic displacement parameters U (in Å^2) for the tetragonal (SG $I4/mmm$) and orthorhombic (SG $Fmmm$) models at 2.4 K, according to the present single-crystal neutron diffraction data. In both SG models $U_{12} = U_{13} = U_{23} = 0$.

SG	Atom	x	y	z	U_{11}	U_{22}	U_{33}	U_{iso}
$I4/mmm$	Ho	0	0	0	0.0008(3)	U_{11}	0.0006(4)	0.00071(19)
	Ni	0	0.5	0.25	0.0029(3)	U_{11}	0.0028(3)	0.00286(17)
	B	0	0	0.35851(10)	0.0046(3)	U_{11}	0.0033(4)	0.00418(18)
	C	0	0	0.5	0.0034(4)	U_{11}	0.0026(5)	0.00310(30)
$Fmmm$	Ho	0	0	0	0.0019(4)	0.0006(6)	0.0005(3)	0.00100(17)
	Ni	0.25	0.25	0.25	0.0057(7)	0.0007(5)	0.0028(2)	0.00310(30)
	B	0	0	0.35854(8)	0.0068(14)	0.0036(12)	0.0033(3)	0.00460(60)
	C	0	0	0.5	0.0020(20)	0.0060(20)	0.0025(4)	0.00340(98)

compounds with angles $\gtrsim$106°–107° show superconductivity. In our low-temperature experiment on $HoNi_2B_2C$, all B-Ni-B angles are found to be larger than 107°, in agreement with the above-mentioned observation.

B. Temperature evolution of commensurate antiferromagnetic and crystal structures

In order to follow the temperature evolution of the $HoNi_2B_2C$ commensurate AFM phase with the wave vector $\boldsymbol{k}_1 = (0, 0, 1)$, several intense magnetic and structural Bragg reflections were collected in the temperature range from 1.3 up to 8 K. Figure 3 (top panel) shows the temperature dependences of the normalized integrated intensities of the magnetic Bragg reflections (111) and (100) as an example. With increasing temperature, their intensities do not significantly change up to about 4 K but decrease rapidly approaching T_N. Both peaks have the same behavior.

The integrated intensities I of magnetic Bragg reflections measured with unpolarized neutrons follow the square of the magnetic order parameter in the vicinity of T_N. The experimental data were successfully fitted in the temperature range from $0.85T_N$ to T_N assuming a power law dependence to the equation [36,37]

$$I = I_0\left(\frac{T_N - T}{T_N}\right)^{2\beta}, \quad (1)$$

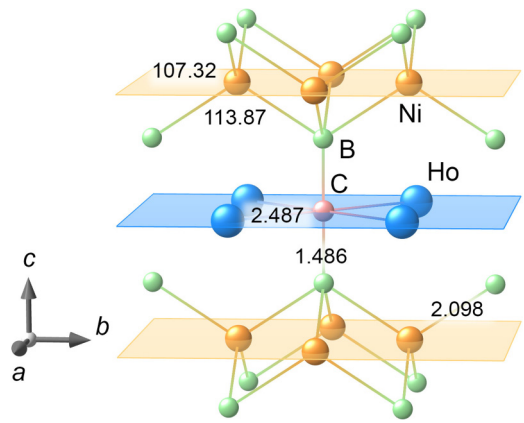

FIG. 2. Selected fragment of the $HoNi_2B_2C$ crystal structure at 2.4 K. Ho-C, B-C, and Ni-B distances are drawn, and their lengths are given in angstroms. B-Ni-B angles (in degrees) are also marked.

where I_0 is the magnetic intensity at $T = 0$ K and β is the critical exponent.

The fit yields $\beta = 0.04 \pm 0.01$, which is significantly smaller even compared to the two-dimensional Ising systems, indicating an effective lowering of dimensionality and fast saturation of the magnetic order parameter in $HoNi_2B_2C$. The fitted Néel temperature of $T_N = 5.16 \pm 0.01$ K is found to be in good agreement with the literature [13,14,18]. We note that the calculated curve corresponds well to the experimental data even below $0.85T_N$ (down to $0.6T_N$), as shown by the dashed line in Fig 3.

Figure 3 (bottom panel) presents the temperature dependences of the normalized integrated intensities of the nuclear Bragg reflections (220), (200), and (0 0 12). An increase of nuclear intensity at low temperatures is ascribed to a change of extinction in the measured single crystal due to magnetoelastic effects in $HoNi_2B_2C$. The onset of the magnetic structure leads to a change of the mosaicity of the crystal and results in increased intensities of Bragg reflections with decreased extinction at low temperature. We note that magnetoelastic effects in $HoNi_2B_2C$ lead also to an orthorhombic distortion (~0.2%) of the tetragonal lattice [18,19]. These large magnetoelastic strains would likely favor the location of magnetic domain walls at crystallographic grain boundaries and dislocations [38,39].

The above-mentioned effect has already been observed in the case of $HoNi_2B_2C$ in the measurements on single crystals [13]. Both in our case and in previous experiments [13], a pure nuclear origin of, e.g., the (200) Bragg reflection is confirmed by polarized neutron diffraction measurements, which allows us to separate the nuclear and magnetic scattering. Within experimental precision no magnetic contribution is detected at Bragg positions with $h + k + l = 2n$ ($n \in \mathbb{Z}$). Moreover, no increase of the nonsplit nuclear peaks is found in the neutron diffraction measurements of the $HoNi_2B_2C$ powder sample [18,19]. As a result, the increase in the intensities of the nuclear Bragg reflections in our single-crystal diffraction measurements can be purely ascribed to a change of the mosaicity of the crystal.

Systematic comparison of the nuclear Bragg peak intensities measured at different temperatures below and above the magnetic phase transition reveals that the strongest effect is found for the reflections in the ab plane, especially those with the scattering vector along the magnetic moments direction. On the other hand, no change is observed for the

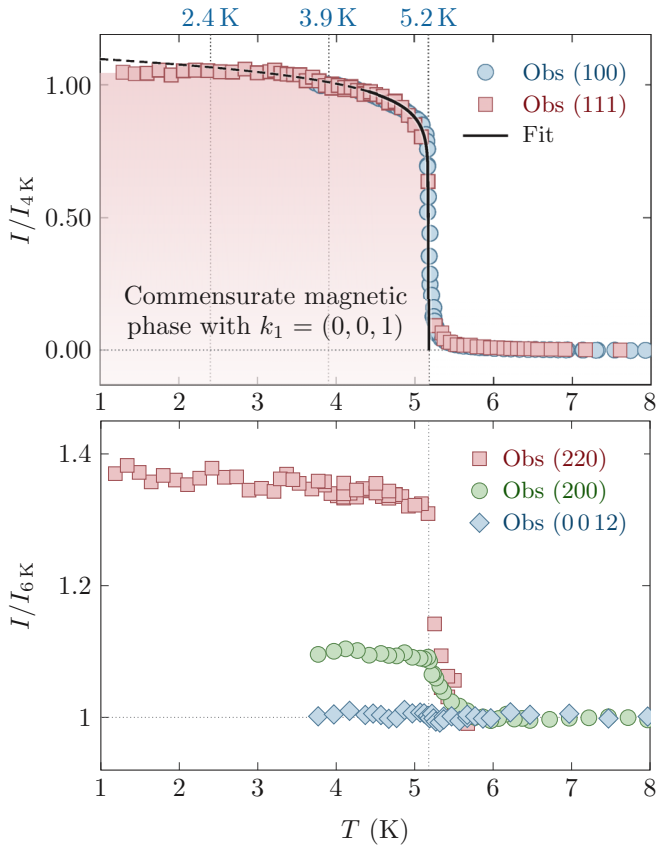

FIG. 3. Top: Temperature dependences of the normalized integrated intensities of the magnetic Bragg reflections (111) and (100). Symbols correspond to unpolarized single-crystal neutron diffraction data. The solid line shows a fit to Eq. (1) in the vicinity (down to $0.85T_N$, $T_N \approx 5.2$ K) of the transition to the commensurate AFM state with $\boldsymbol{k}_1 = (0, 0, 1)$. The dashed line is an extension of the fit curve below $0.85T_N$. Temperatures of SNP measurements (3.9 K) described in Sec. III D and unpolarized neutron diffraction studies (2.4 K) described in Sec. III C are indicated. Bottom: Temperature dependences of the normalized integrated intensities of the nuclear Bragg reflections (220), (200), and (0 0 12).

perpendicular direction c (Fig. 3, bottom panel), where the magnetic component is zero. This indicates that the change of mosaicity (or extinction) is anisotropic at low temperatures and agrees well with our and the literature [13,15] temperature dependencies of nuclear Bragg peaks. Thus, the observed extinction effects give us additional information about the increase of anisotropic strain effects, which are locally induced in the $HoNi_2B_2C$ single crystal at low temperatures. This mosaicity change is caused by the strong magnetoelastic coupling, which is also a source of the symmetry reduction in $HoNi_2B_2C$.

C. Magnetic structure models by symmetry analysis and unpolarized neutron diffraction

In order to solve the magnetic structure of $HoNi_2B_2C$ we used the concept of Shubnikov groups (magnetic space groups), which is very useful in the case of second-order phase transitions for enumerating the possible magnetic structures compatible with the parent crystal symmetry. This approach implies specific symmetry-deduced constraints on the magnetic moments. That is, the magnetic moments of symmetry-equivalent atoms are related via the magnetic symmetry operations. The approach allows one to reduce the number of refined parameters and to average the symmetry-equivalent reflections. It was shown that the use of MSGs significantly facilitates the interpretation of the results (see, e.g., Ref. [40] and references therein).

The possible magnetic structures are obtained based on two models of the parent nuclear structure, namely, orthorhombic $Fmmm$ and tetragonal $I4/mmm$, as discussed in Sec. III A.

First, we consider that the nonmagnetic parent space group of $HoNi_2B_2C$ is $Fmmm$. In this case, its corresponding gray group is $Fmmm1'$, which, in addition, includes the time reversal operation. The symmetry of a magnetically ordered phase is described by a subgroup of this parent group. Figure 4 (left panel) shows the k-maximal subgroups [40] for $Fmmm1'$ with the magnetic propagation vector $\boldsymbol{k} = (0, 0, 1)$. Only three subgroups which allow nonzero magnetic moments are possible. The first one (MSG C_Accm) forces an alignment of the spins of Ho parallel to the c axis and, as a result, fails to reproduce our experimental neutron diffraction data and disagrees with the results of the macroscopic magnetization measurements [41]. This implies that the magnetic space group cannot be tetragonal and has to be of lower symmetry. The last two subgroups (MSG C_Amca) differ only by the interchange of the a and b axes, as can be seen from the diagram. In both cases, only trivial magnetic domains with all spins reversed (180° domains) are possible. However, a reduction of the symmetry from tetragonal SG $I4/mmm$ to orthorhombic SG $Fmmm$ implies the loss of the fourfold rotation axis, which can be treated as an additional twin operation with respect to a diagonal mirror plane (90° twin domains). As a result, these two magnetic structures can be combined into a single magnetic model with MSG C_Amca and two types of 90° magnetic domains that correspond to the magnetic ordering along the a or b axis.

The same procedure was applied to select the magnetic structures considering $I4/mmm$ as the nonmagnetic parent SG. Figure 4 (right panel) shows the k-maximal subgroups [40] for the corresponding gray group $I4/mmm1'$ with the magnetic propagation vector $\boldsymbol{k} = (0, 0, 1)$. Again, the MSG P_I4/mnc is ruled out, as it allows the magnetic moments to be aligned along only the c axis. Two other MSGs constrain Ho moments to lie in the ab plane. Those are MSG P_Innm (Ho spins are along the [100] direction of the parent structure) and MSG C_Amca (Ho spins are along the [110] of the parent structure). In both cases, two types of 90° magnetic domains are possible. We note that the MSG C_Amca model (with magnetic domains) derived from the parent SG $I4/mmm$ coincides with that derived from the parent SG $Fmmm$.

A further reduction of the symmetry from the parent SG $I4/mmm$ leads to the monoclinic MSG P_A2_1/c, which allows a free rotation of the moment in the ab plane. However, it increases the number of free parameters without significantly improving the quality of the fit. Therefore, refinements assuming nonmaximal subgroups were discarded.

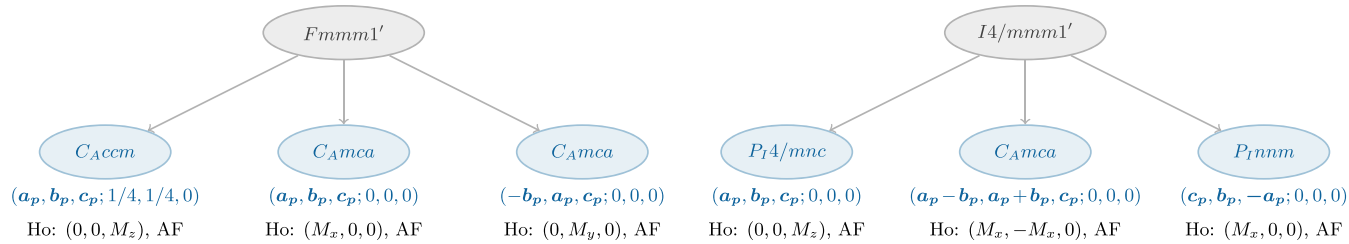

FIG. 4. The possible k-maximal symmetries for a magnetic ordering of Ho with propagation vector $\boldsymbol{k} = (0, 0, 1)$ on a paramagnetic phase with (left panel) SG $Fmmm$ and its corresponding gray group $Fmmm1'$ and (right panel) SG $I4/mmm$ and its corresponding gray group $I4/mmm1'$. Only the subgroups which allow nonzero magnetic moments are shown. Each magnetic space group label is shown together with the transformation from the corresponding parent unit cell basis $\{\boldsymbol{a}_p, \boldsymbol{b}_p, \boldsymbol{c}_p\}$ to its standard setting. The allowed magnetic moment components on the Ho atoms which correspond to the AFM ordering are given at the bottom.

Moreover, an inclination of Ho moments out of the *ab* plane suggested in Ref. [17] is forbidden by symmetry even in the monoclinic MSG because the in-plane (*ab*) and out-of-plane (*c*) components are not allowed simultaneously.

Thus, the choice of the magnetic symmetry in the case of $HoNi_2B_2C$ is simplified to the selection between the models with Ho moments along either side [100] or diagonal [110] directions of the parent tetragonal structure that corresponds to MSG P_Innm or C_Amca, respectively. Both types of magnetic structures are shown in Figs. 5(a) and 5(b). It is, however, difficult to distinguish between those two MSGs on the basis of the conventional unpolarized neutron diffraction data if the 90° magnetic domains are equally populated or just slightly imbalanced. The presence of such domains of micrometer size in $HoNi_2B_2C$ was experimentally proved by using the high-resolution Bitter decoration technique [42]. Figures 5(c) and 5(d) show the neutron diffraction data fit quality using both the MSG C_Amca and MSG P_Innm models. A small imbalance of 90° twin domains is found. The twin volume ratio as determined from structure refinement is 43/57, with a standard deviation of less than 2%. Nevertheless, the goodness of fit of the refinement based on the unpolarized neutron diffraction data is similar for both magnetic structure models, as can be seen by a comparison of Figs. 5(c) and 5(d). On the other hand, polarized neutrons can be much more sensitive to the model differences, even in the case of a small domain imbalance, due to the presence of the nuclear-magnetic interference term. In order to unambiguously solve the magnetic structure of $HoNi_2B_2C$, we performed spherical neutron polarimetry measurements on the same single crystal which showed that the correct model is described by MSG C_Amca (see Sec. III D).

The magnitude of the ordered magnetic moment on Ho was found to be 9.16(9) μ_B at 2.4 K (commensurate AFM phase, Fig. 3), which is comparable to values reported in the literature of approximately 8.6 μ_B–9.1 μ_B, according to neutron powder diffraction measurements [8,11,13,17]. This value lies below the free-ion value of 10.4 μ_B, indicating that crystal field effects are important [10].

No significant magnetic moment was refined for the Ni atoms, possibly indicating the high level of independence between the Ho and Ni sublattices.

D. Unambiguous magnetic structure solution by spherical neutron polarimetry

In a polarized neutron scattering experiment the relationship between the polarization of the incident ($\boldsymbol{P}$) and scattered ($\boldsymbol{P'}$) beams can be expressed conveniently by the tensor equation [43]:

$$\boldsymbol{P'} = \mathbf{P}\boldsymbol{P} + \boldsymbol{P''}$$

or in components

$$P'_i = \mathsf{P}_{ij} P_j + P''_i,$$

where tensor $\mathbf{P}$ describes the rotation of the polarization, while $\mathbf{P}''$ is the polarization created in the scattering process.

SNP can distinguish between polarization rotation and depolarization of the neutron beam occurring upon scattering from the lattice of the ordered moments. It precisely determines the direction of the magnetic interaction vector, which is the projection of the magnetic structure factor onto the plane perpendicular to the scattering vector Q. A more detailed description of the SNP technique can be found elsewhere [44]. The experimental quantities obtained in an SNP experiment for each Bragg reflection are the components $\mathcal{P}_{ij}$ of the 3×3 polarization matrix $\boldsymbol{\mathcal{P}}$,

$$\mathcal{P}_{ij} = \frac{I_{ij}^{++} - I_{ij}^{+-}}{I_{ij}^{++} + I_{ij}^{+-}},$$

where the indices i and j refer to one of the three orthogonal directions x, y, and z defined during the experiment. The first subscript corresponds to the direction of the initial polarization vector, while the second is the direction of analysis. I is the measured intensity with polarization parallel (++) and antiparallel (+−) to j.

The polarization matrix is closely related to the polarization tensor as

$$\mathcal{P}_{ij} = \left\langle \frac{P_i \mathsf{P}_{ij} + P''_j}{P_i} \right\rangle_{\text{domains}},$$

where the brackets indicate an average over all the different magnetic domains which contribute to the reflection.

In the case of $HoNi_2B_2C$ the magnetic domains rotated by 90° with respect to each other are allowed by symmetry in

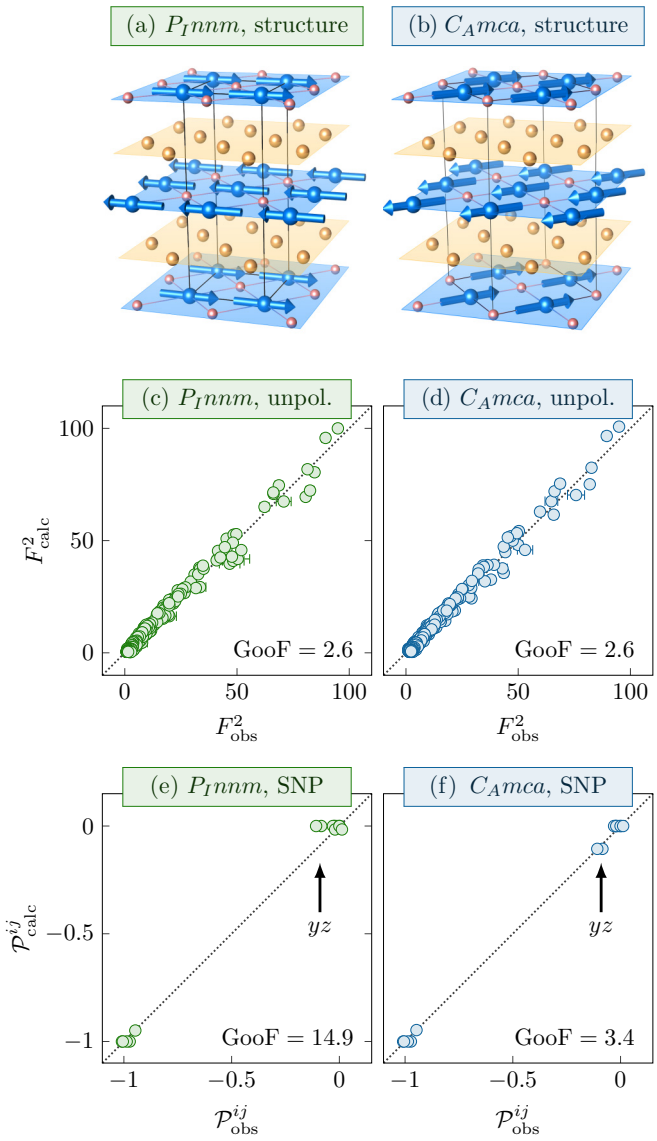

FIG. 5. Magnetic structure of $HoNi_2B_2C$ in (a) MSG $P_I nnm$ and (b) MSG $C_A mca$. Boron atoms are not shown for simplicity. Quality of the unpolarized neutron diffraction data refinement at 2.4 K in (c) MSG $P_I nnm$ and (d) MSG $C_A mca$. The experimental structure factors squared $F^2_{\rm obs}$ are plotted against the calculated ones $F^2_{\rm calc}$. The quality of the spherical neutron polarimetry data refinement at 3.9 K is shown in (e) MSG $P_I nnm$ and (f) MSG $C_A mca$. The experimental polarization matrix elements $\mathcal{P}^{ij}_{\rm obs}$ are plotted against the calculated ones $\mathcal{P}^{ij}_{\rm calc}$.

both the $C_A mca$ and $P_I nnm$ cases, as described in Sec. III C. If one type is dominant, nonzero terms occur in three elements of the polarization matrix: one diagonal (xx) and two off diagonal (yz, zy) for MSG $C_A mca$ and just three diagonal (xx, yy, zz) ones for MSG $P_I nnm$ (see Figs. S2(a)–S2(c) in the Supplemental Material [34]). Thus, there is a clear difference between these two types of MSGs. However, in the case of equal domain population the resulting polarization matrices (after averaging through the domains) become identical for both MSG $C_A mca$ and MSG $P_I nnm$ as they contain only a single nonzero diagonal term (xx; see Fig. S2(d) in the Supplemental Material [34]).

In order to determine the magnetic domain population and the MSG of $HoNi_2B_2C$, neutron polarimetry measurements were performed on a single crystal with a vertically oriented [010] axis at 3.9 K (the commensurate AFM phase, Fig. 3). This geometry gave access to ($h0l$)-type reflections. Figures 5(e) and 5(f) show the differences between the experimentally measured and calculated elements of the polarization matrices for some magnetic Bragg reflections. The experimental off-diagonal yz terms are not zero. This is a clear indication that the $P_I nnm$-type magnetic model, for which only diagonal elements exist, fails to reproduce the measured data. On the other hand, the $C_A mca$-type magnetic model with unequal domain populations agrees well with the SNP experimental data. Our result confirms the model proposed in Refs. [8,18].

To determine the precise domain population ratio in the measured sample, we collected the full polarization matrices of the magnetic reflections (100), (201), (003), and (005) and some of their symmetry equivalents. Based on these data, a magnetic domain ratio of 45/55 with a standard deviation of less than 1% was found from least-squares refinement. This volume ratio of AFM domains as determined by SNP corresponds to that of the orthorhombic twins (43/57) determined independently by crystal structure refinement.

Thus, even in the case of a small domain imbalance, the SNP measurements allow us to unambiguously distinguish between the two models of magnetic structure deduced from unpolarized neutron diffraction.

According to Ref. [42], a vortex band structure is formed below the incommensurate-to-commensurate AFM transition temperature in the superconducting state of $HoNi_2B_2C$. The vortices observed on the surface are aligned along the domain walls in the directions [100] and [010]. Using SNP, the populations of the different AFM domains were determined in the bulk of the crystal. The direct evidence of the domain imbalance in $HoNi_2B_2C$ is a finding which was not addressed in previous studies and may be relevant for a better understanding of the tight interplay between magnetic and superconducting properties in the title compound.

IV. SUMMARY

$HoNi_2B_2C$ has attracted much attention in recent decades because of the coexistence of superconductivity and magnetic order as well as near-reentrant superconducting to resistive and back to superconducting behavior where its magnetic order changes from the incommensurate to commensurate one (Ref. [2] and references therein). Previous neutron diffraction studies on $HoNi_2B_2C$ failed to unambiguously determine the absolute direction of the Ho magnetic moments in the tetragonal ab plane due to the technique's limitations related to the existence of magnetic domains. An easy magnetization axis was proposed based on separate macroscopic magnetization measurements. In the present work we showed that the $HoNi_2B_2C$ magnetic structure can be directly and unambiguously determined using spherical neutron polarimetry as the only technique. The magnetic moments of the Ho-atoms were found to be aligned along [110] in the parent body centered tetragonal cell of the high-temperature phase. The refined magnitude of the ordered moment is 9.16(9) μ_B/Ho^{3+} atom.

Our results confirm the suggestions made in Refs. [8,41] and rule out other models proposed in Refs. [10,11,17]. Our detailed symmetry analysis allowed us to determine the magnetic space group of $HoNi_2B_2C$ to be C_Amca with two types of 90° AFM domains. The nonequilibrium volume ratio of AFM domains in the superconducting phase was demonstrated and quantitatively determined. It should be noted that the domain structure influences the superconducting properties (vortex lattice) as the vortices are aligned along the domain walls [40].

A structural distortion due to the magnetoelastic effect leads to the tetragonal-to-orthorhombic symmetry lowering previously reported for $HoNi_2B_2C$ [18,19]. However, the structural parameters of the orthorhombic phase have never been published, although this information is important from both experimental and theoretical points of view for the description of the superconductivity. Here, the precise structural parameters of $HoNi_2B_2C$ in the AFM superconducting phase (at 2.4 K) were presented for both the low-symmetry orthorhombic (SG $Fmmm$) and high-symmetry tetragonal (SG $I4/mmm$) structural models, as determined by the single-crystal neutron diffraction technique. The fit quality of our experimental data at low temperatures is comparable for both models, although reliability factors are slightly better in the case of the orthorhombic structure. SNP measurements allowed us to discover a pure magnetic origin of the intensities occurring at the forbidden positions and thus to discard other nuclear structural models with lower symmetry. Magnetic symmetry analysis showed that the experimentally observed magnetic structure is compatible with both tetragonal and orthorhombic parent crystal symmetries.

In addition, the exact temperature dependence of both the nuclear and magnetic Bragg reflections were measured through the AFM transition. The critical exponent related to the ordered phase was found to be anomalously small, indicating an effective lowering of dimensionality and fast saturation of the magnetic order parameter in $HoNi_2B_2C$. The magnetic phase transition was found to be accompanied by the significant change of mosaicity (or extinction), in agreement with previous studies. However, our detailed and systematic studies of different reflections showed that mosaicity becomes strongly anisotropic at low temperatures, with the strongest effect in the $(hh0)$-type reflections, whereas the $(00l)$ direction is hardly affected at all. Taking into account that the Ho magnetic moments are aligned along [110], such an anisotropy of mosaicity can serve as an additional argument in favor of orthorhombic distortion caused by the strong magnetoelastic coupling in $HoNi_2B_2C$.

ACKNOWLEDGMENTS

The work was supported by the German Federal Ministry for Education and Science (BMBF) through projects 03HE7AAC, 03HE6AA3, and 05K10PA2. Part of the work is based upon experiments performed at the HEiDi and POLI instruments at Heinz Maier-Leibnitz Zentrum (MLZ), Garching, Germany, operated by RWTH Aachen in cooperation with Forschungszentrum Jülich GmbH (Jülich Aachen Research Alliance, JARA).

[1] R. J. Cava, H. Takagi, H. W. Zandbergen, J. J. Krajewski, W. F. Peck, Jr., T. Siegrist, B. Batlogg, R. B. van Dover, R. J. Felder, K. Mizuhashi, J. O. Lee, H. Eisaki, and S. Uchida, Nature (London) **367**, 252 (1994).

[2] K.-H. Müller and V. N. Narozhnyi, Rep. Prog. Phys. **64**, 943 (2001).

[3] L. Dezaneti, Y. Xue, Y. Sun, K. Ross, and C. Chu, Phys. C (Amsterdam, Neth.) **334**, 123 (2000).

[4] H. Eisaki, H. Takagi, R. J. Cava, B. Batlogg, J. J. Krajewski, W. F. Peck, Jr., K. Mizuhashi, J. O. Lee, and S. Uchida, Phys. Rev. B **50**, 647 (1994).

[5] Z. Ban and M. Sikirica, Acta Crystallogr. **18**, 594 (1965).

[6] T. Siegrist, R. J. Cava, J. J. Krajewski, and W. F. Peck, Jr., J. Alloys Compd. **216**, 135 (1994).

[7] T. Siegrist, H. W. Zandbergen, R. J. Cava, J. J. Krajewski, and W. F. Peck, Jr., Nature (London) **367**, 254 (1994).

[8] J. W. Lynn, S. Skanthakumar, Q. Huang, S. K. Sinha, Z. Hossain, L. C. Gupta, R. Nagarajan, and C. Godart, Phys. Rev. B **55**, 6584 (1997).

[9] U. Jaenicke-Roessler, A. Belger, G. Zahn, B. Wehner, P. Paufler, and H. Bitterlich, Phys. C (Amsterdam, Neth.) **314**, 43 (1999).

[10] T. E. Grigereit, J. W. Lynn, Q. Huang, A. Santoro, R. J. Cava, J. J. Krajewski, and W. F. Peck, Jr., Phys. Rev. Lett. **73**, 2756 (1994).

[11] Q. Huang, A. Santoro, T. E. Grigereit, J. W. Lynn, R. J. Cava, J. J. Krajewski, and W. F. Peck, Jr., Phys. Rev. B **51**, 3701 (1995).

[12] J. Freudenberger, G. Fuchs, K. Nenkov, A. Handstein, M. Wolf, A. Kreyssig, K.-H. Müller, M. Loewenhaupt, and L. Schultz, J. Magn. Magn. Mater. **187**, 309 (1998).

[13] M. Schneider, O. Zaharko, U. Gasser, A. Kreyssig, P. J. Brown, and P. C. Canfield, Phys. Rev. B **74**, 104426 (2006).

[14] E. Alleno, S. Singh, S. K. Dhar, and G. André, New J. Phys. **12**, 043018 (2010).

[15] A. I. Goldman, C. Stassis, P. C. Canfield, J. Zarestky, P. Dervenagas, B. K. Cho, D. C. Johnston, and B. Sternlieb, Phys. Rev. B **50**, 9668 (1994).

[16] J. P. Hill, B. J. Sternlieb, D. Gibbs, C. Detlefs, A. I. Goldman, C. Stassis, P. C. Canfield, and B. K. Cho, Phys. Rev. B **53**, 3487 (1996).

[17] C. Tomy, L. Chang, D. M. Paul, N. Andersen, and M. Yethiraj, Phys. B (Amsterdam, Neth.) **213–214**, 139 (1995).

[18] A. Kreyssig, M. Loewenhaupt, J. Freudenberger, K.-H. Müller, and C. Ritter, J. Appl. Phys. **85**, 6058 (1999).

[19] A. Kreyssig, A. Schneidewind, M. Loewenhaupt, C. Ritter, J. Freudenberger, G. Fuchs, and K.-H. Müller, in *Rare Earth Transition Metal Borocarbides (Nitrides): Superconducting, Magnetic and Normal State Properties*, edited by K.-H. Müller and V. Narozhnyi (Springer, Dordrecht, 2001), pp. 181–186.

[20] C. Detlefs, A. H. M. Z. Islam, T. Gu, A. I. Goldman, C. Stassis, P. C. Canfield, J. P. Hill, and T. Vogt, Phys. Rev. B **56**, 7843 (1997).
[21] C. Song, Z. Islam, L. Lottermoser, A. I. Goldman, P. C. Canfield, and C. Detlefs, Phys. Rev. B **60**, 6223 (1999).
[22] E. Lelièvre-Berna, E. Bourgeat-Lami, P. Fouilloux, B. Geffray, Y. Gibert, K. Kakurai, N. Kernavanois, B. Longuet, F. Mantegezza, M. Nakamura, S. Pujol, L.-P. Regnault, F. Tasset, M. Takeda, M. Thomas, and X. Tonon, Phys. B (Amsterdam, Neth.) **356**, 131 (2005).
[23] D. Souptel, G. Behr, A. Kreyssig, and W. Löser, J. Cryst. Growth **276**, 652 (2005).
[24] G. Behr, W. Löser, D. Souptel, G. Fuchs, I. Mazilu, C. Cao, A. Köhler, L. Schultz, and B. Büchner, J. Cryst. Growth **310**, 2268 (2008).
[25] D. Souptel, Ph.D. thesis, TU Dresden, 2005.
[26] Stoe and Cie, X-AREA, Darmstadt, Germany, 2002.
[27] M. Meven and A. Sazonov, J. Large-Scale Res. Facil. **1**, A7 (2015).
[28] A. P. Sazonov, DAVINCI: Software for visualization and processing of single-crystal diffraction data measured with a point detector, http://davinci.sazonov.org.
[29] V. Petříček, M. Dušek, and L. Palatinus, Z. Kristallogr. **229**, 345 (2014).
[30] V. Hutanu, W. Luberstetter, E. Bourgeat-Lami, M. Meven, A. Sazonov, A. Steffen, G. Heger, G. Roth, and E. Lelièvre-Berna, Rev. Sci. Instrum. **87**, 105108 (2016).
[31] V. Hutanu, J. Large-Scale Res. Facil. **1**, A16 (2015).
[32] V. Hutanu, M. Meven, S. Masalovich, G. Heger, and G. Roth, J. Phys.: Conf. Ser. **294**, 012012 (2011).
[33] P. J. Brown and J. C. Matthewman, *The Cambridge Crystallography Subroutine Library Users' Manual* (IAEA, UK, 2009).
[34] See Supplemental Material at http://link.aps.org/supplemental/10.1103/PhysRevB.100.014414 for the details of the crystal structure refinement at room temperature by neutron and x-ray diffraction, a comparison between tetragonal and orthorhombic structural models at low temperature, and the influence of antiferromagnetic domain population on the spherical neutron polarimetry data.
[35] Inorganic Crystal Structure Database, CCD Numbers 1935768-1935770, http://www.fiz-karlsruhe.de.
[36] T. Chatterji, *Neutron Scattering from Magnetic Materials* (Elsevier, Amsterdam, 2006), p. 572.
[37] E. E. Rodriguez, C. Stock, K. L. Krycka, C. F. Majkrzak, P. Zajdel, K. Kirshenbaum, N. P. Butch, S. R. Saha, J. Paglione, and M. A. Green, Phys. Rev. B **83**, 134438 (2011).
[38] L. Y. Vinnikov, J. Anderegg, S. L. Bud'ko, P. C. Canfield, and V. G. Kogan, JETP Lett. **77**, 502 (2003).
[39] L. Y. Vinnikov, I. S. Veshchunov, S. L. Bud'ko, P. C. Canfield, and V. G. Kogan, J. Phys.: Conf. Ser. **150**, 052279 (2009).
[40] J. M. Perez-Mato, S. V. Gallego, E. S. Tasci, L. Elcoro, G. de la Flor, and M. I. Aroyo, Annu. Rev. Mater. Res. **45**, 217 (2015).
[41] P. C. Canfield, B. K. Cho, D. C. Johnston, D. K. Finnemore, and M. F. Hundley, Phys. C (Amsterdam, Neth.) **230**, 397 (1994).
[42] L. Y. Vinnikov, J. Anderegg, S. L. Bud'ko, P. C. Canfield, and V. G. Kogan, Phys. Rev. B **71**, 224513 (2005).
[43] P. J. Brown, Phys. B (Amsterdam, Neth.) **297**, 198 (2001).
[44] P. J. Brown, in *Neutron Scattering from Magnetic Materials*, edited by T. Chatterji (Elsevier, Amsterdam, 2006), pp. 215–244.